Compact −300 kV dc inverted insulator photogun with biased anode and alkali-antimonide photocathode

C. Hernandez-Garcia,* P. Adderley, B. Bullard, J. Benesch, J. Grames, J. Gubeli, F. Hannon, J. Hansknecht, J. Jordan, R. Kazimi, G. A. Krafft, M. A. Mamun, M. Poelker, M. L. Stutzman, R. Suleiman, M. Tiefenback, Y. Wang, and S. Zhang
Thomas Jefferson National Accelerator Facility, Newport News, Virginia 23606, USA

H. Baumgart, G. Palacios-Serrano, S. Wijethunga, and J. Yoskowitz
Old Dominion University, Norfolk, Virginia 23529, USA

C. A. Valerio Lizarraga
Facultad de Ciencias Físico-matemáticas Universidad Autónoma de Sinaloa, Culiacán 80010, Mexico

R. Montoya Soto
Departamento de Física, Universidad de Guanajuato, León 37150, Mexico

A. Canales Ramos
Universidad Nacional Autónoma de Mexico, Mexico City 04510, Mexico

(Received 13 August 2019; published 13 November 2019; corrected 30 January 2020)

This contribution describes the latest milestones of a multiyear program to build and operate a compact −300 kV dc high voltage photogun with inverted insulator geometry and alkali-antimonide photocathodes. Photocathode thermal emittance measurements and quantum efficiency charge lifetime measurements at average current up to 4.5 mA are presented, as well as an innovative implementation of ion generation and tracking simulations to explain the benefits of a biased anode to repel beam line ions from the anode-cathode gap, to dramatically improve the operating lifetime of the photogun and eliminate the occurrence of micro-arc discharges.

DOI: 10.1103/PhysRevAccelBeams.22.113401

I. INTRODUCTION

State-of-the-art dc high voltage photoemission guns operate at negative bias voltage in the range of 100 to 400 kV and with electric field strengths of the order of 10 MV/m to provide bright electron beams for a variety of accelerator applications. Nuclear physics experiments like those conducted at Jefferson Lab Continuous Electron Beam Accelerator Facility (CEBAF) rely on dc high voltage photoemission guns to produce highly polarized electron beams at currents ∼100 μA from negative electron affinity GaAs-based photocathodes that demand superb vacuum conditions to achieve long photocathode operational lifetime [1,2]. Other accelerator applications that use dc high voltage photoemission guns such as free electron lasers [3], energy recovery linacs [4,5] and electron cooling [6,7] require unpolarized electron beams with high bunch charge and high average current of the order of tens to hundreds of mA. For these high-current unpolarized beam applications, alkali-antimonide photocathodes are today's photocathodes of choice [8].

To operate reliably, it is essential that dc high voltage photoemission guns exhibit little or no field emission [9,10]. Low-level field emission at nA levels desorbs gas from the vacuum chamber walls by direct impact and by x-ray stimulated desorption, leading to enhanced ion bombardment of the photocathode which hastens quantum efficiency decay [11]. Field emission at the μA level can lead to high voltage breakdown often resulting in irreparable damage of the photogun insulator [12].

A number of dc high voltage photoemission guns (photoguns hereafter) rely on large cylindrical ceramic insulators to electrically isolate the cathode electrode [13–15], which must be supported on a long coaxial metal support tube. A symmetric-field vent-and-bake version of this type of photogun operating at −350 kV demonstrated 500 Coulomb quantum efficiency (QE) 1/e charge lifetime

*chgarcia@jlab.org

while delivering up to 8 mA from a bulk GaAs photocathode for the Jefferson Lab free electron laser (FEL), which set many records including the highest optical output power from an FEL at millimeter, infrared and ultraviolet wavelengths, and achieving at the time the highest average beam current in an energy recovery linac from a dc high voltage photogun [16]. Another example is the Cornell photogun in Ref. [17] which demonstrated a world record 65 mA average current employing a vertically mounted cylindrical insulator, thus allowing the use of a load-lock system to exchange photocathodes. A copy of the Cornell photogun is in operation at Brookhaven National Laboratory and routinely delivers tens of milliamperes average current for the LEReC experiment [7], while a similar photogun design at KEK in Japan has recently demonstrated sustained ∼1 mA cw electron beam from GaAs photocathodes biased at −500 kV [18].

II. EXPERIMENTAL SETUP

A. Photogun

In contrast to these designs, a photogun with an inverted insulator geometry was chosen to support R&D related to the Jefferson Lab Electron Ion Collider recirculator-cooler project [19], specifically aimed at studying the production of magnetized electron beam with nano-Coulomb bunch charge and at high average current. This new photogun is a larger version of the −130 kV CEBAF load-locked photogun that has functioned reliably for years [20]. The inverted-insulator design was chosen for several technical reasons: it provides a small volume which can result in better achievable vacuum since there is less surface area contributing gas load, the insulator serves as the electrode support structure which means there is less metal biased at high voltage contributing to field emission [21], and lastly high voltage is applied to the cathode electrode using a commercial high voltage cable with a termination designed to mate with the inverted geometry insulator, which means there is no exposed high voltage and thus, an SF_6 tank is not required to suppress corona discharge at the photogun. There were also practical considerations related to the choice of the ceramic insulator. The comparatively small ceramic insulators are considerably less expensive than the large segmented cylindrical insulators used on other photoguns, and because the photogun is smaller and connected to the power supply with a cable, the photogun and high voltage power supply can be positioned relatively independently of each other.

This contribution discusses the photogun electrostatic design which incorporates a triple-point junction shield used to linearize the potential across the length of the insulator [22], the performance of barrel-polished electrodes [23], the alkali-antimonide photocathode deposition chamber and load-lock features that permit rapid photocathode replacement, the diagnostic beam line and

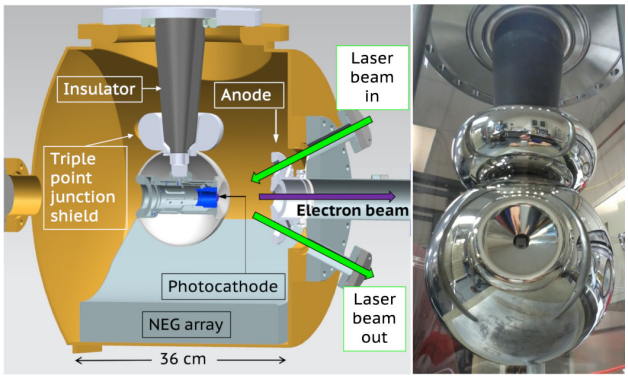

FIG. 1. Left: Cross-section view of the −300 kV photogun with inverted geometry ceramic insulator (dark grey). The photocathode (purple) and puck (blue) sit inside the spherical cathode electrode with Pierce focusing element. The laser light is shown in the vertical plane but, in practice, the laser light illuminates the photocathode in the horizontal plane. Right: Photograph of the centrifugal barrel-polished cathode assembly (spherical and screening electrodes) mounted to a doped alumina inverted insulator on a 25 cm diameter ConFlat® flange.

emittance measurement techniques used to measure geometric emittance of the beam produced across the full active area of the photocathode and to evaluate the intrinsic thermal emittance of Cs_xK_ySb photocathodes fabricated on GaAs substrates [24,25], and an rf-pulsed green-light drive laser that employs an extremely versatile and reliable gain-switched diode laser master oscillator and fiber amplifiers. Importantly, this contribution describes a highly successful method to prolong photocathode QE lifetime using a biased anode to minimize ion bombardment of the photocathode by repelling ions produced in the beam line. At sufficient voltage, the biased anode completely eliminated high voltage micro-arc discharges that resulted in significant stepwise QE decay. Simulations are presented that explain the benefits of the biased anode in terms of diminished ion bombardment of the photocathode.

A schematic of the −300 kV photogun is shown in Fig. 1 together with a photograph of the cathode electrode attached to the narrow end of a tapered conical insulator. The spherical cathode includes a specially designed screening electrode that reduces the field strength at the triple-point junction where arcing is thought to originate [22]. The cathode electrode was made of two 15.2 cm diameter hydroformed hemispherical shells (316L stainless steel) welded together. The assembly composed of spherical body and screening electrode was barrel polished to achieve a mirrorlike surface finish using two types of abrasives, with total polishing time of just a few hours [23]. Another key feature of the photogun design is the manner in which the drive laser beam is delivered to the photocathode. Rather than illuminating the photocathode at nearly normal incidence which is typical of most photogun systems, the drive laser beam passes through entrance and exit holes in the

anode electrode at a 25° angle of incidence, thereby eliminating the need for in-vacuum laser mirrors which can restrict the effective aperture of the beam line (a large beam line aperture was desired for high average current and high bunch charge beam delivery). In addition, the viewports on the anode assembly flange have a broadband antireflection coating to minimize scattered laser light which can generate halo. The anode is also electrically isolated from ground potential to enable measurement of field emission from the cathode electrode and to enable biasing as a means to repel downstream ions created by the beam [26]. Some of these design features are discussed in more detail below.

The narrow end of the conical insulator passes through a hole in the spherical cathode electrode and mates to an internal fixture that holds a photocathode puck. The triple-point junction screening electrode was captured by the insulator and firmly attached to the spherical cathode electrode using set screws. The spherical electrode possesses a front face with 1.2 cm opening and 25° Pierce focusing geometry. Spring-loaded sapphire rollers push the photocathode puck against the back of the focusing faceplate. Interior components of the electrode are held in place using a rear hemitoroidal faceplate designed to minimize the electrostatic field strength.

The photogun vacuum chamber is made of 304L stainless steel 0.5 cm thick. Prior to assembly, the empty chamber was vacuum baked at 400 °C for 100 hours to reduce outgassing from the chamber walls [27]. The resulting outgassing rate was $\sim 2 \times 10^{-13}$ Torr l/s/cm^2 measured using a spinning rotor gauge. Upon completion of outgassing measurements, the vacuum chamber was moved to a class 1000 clean room where the photogun was fully assembled. The bottom half of the gun chamber includes an array of eight nonevaporable getter (NEG) pump modules (SAES WP1250 with ST707 material) to provide an estimated pump speed of ∼4000 l/s for hydrogen, which is the dominant gas species inside the vacuum chamber. A perforated ground screen covers the modules to minimize the likelihood of NEG particulates becoming electrostatically charged and attracted to the cathode electrode initiating field emission. An adjustable leak valve mounted to the side of the photogun vacuum chamber provides a means to add krypton gas during high voltage conditioning when field emission is encountered [28]. A 40 l/s ion pump provides pumping for noble gases and gas species like methane and carbon monoxide which are poorly pumped by the NEGs. Additionally the ion pump serves as a vacuum gauge during operation using a highly sensitive current monitor that is integral to the ion pump power supply, which can accurately register sub-nA ion pump currents [29]. The ion pump current was measured to be proportional to pressure through the high 10^{-12} Torr range.

After fabrication, the electrodes were vacuum degassed at 900°C, then barrel polished and cleaned in an ultrasonic bath of 2-propanol. The ceramic was thoroughly cleaned using lint-free wipes that were soaked in 2-propanol. High pressure rinsing was not used on the electrodes. Instead, the insulator-electrode assembly was cleaned using a supersonic jet of CO_2 prior to installation. Other internal components, such as the metal puck holding mechanism and the NEG ground screen, were vacuum degassed to minimize outgassing. Once assembled, the photogun was moved to a radiation shielded enclosure and vacuum baked at 200 °C until the pressure drop measured by an external pumping station was less than 10% in 24 hours. This occurred after ∼100 hours. The NEG modules were activated at 450 °C for 45 minutes at the end of the bake. After a few days, the baseline ion pump current settled at 0.2 nA which is equivalent to a pressure of $\sim 7 \times 10^{-12}$ Torr. The expected pressure based on the assumptions for outgassing rate, surface area, and installed pump speed was $\sim 1 \times 10^{-12}$ Torr. The higher than expected pressure is likely due to the NEG shield screen which reduces the effective pump speed of the NEG modules.

Following the vacuum bake, the photogun was high voltage conditioned to eliminate field emission at the desired operating voltage, −300 kV. The photogun was connected to a −500 kV dc Cockcroft-Walton SF_6 gas insulated high voltage power supply (HVPS), with a 300 MΩ current-limiting resistor in series. Male-type cable connectors fit precisely into the conical inverted insulator on the photogun, and into a plastic receptacle (350 kV GEN Wide Band epoxy receptacle by Dielectric Sciences, Inc.) supporting the conditioning resistor inside the HVPS SF_6 tank. The ceramic insulator and the high voltage cable are industry-standard components with dimensions specified by the commercial designation R30. The insulator was fabricated with a vendor-proprietary dopant that provides a small level of conductivity to drain charge that might accumulate on the surface and within the bulk [22]. Initially, voltage was applied to the cathode under vacuum conditions at a rate of 10 kV/ min up to −200 kV, and then in steps of 5 kV at a rate of 1 kV/ min. Figure 2 shows the high voltage conditioning process. The x-ray radiation signal tracks the vacuum activity, with both signals indicating the signature of field emission. At this point, krypton gas was added to the photogun vacuum chamber at pressure $\sim 5 \times 10^{-5}$ Torr, and then voltage was raised at a rate of 4 kV/hr. Gas conditioning serves to eliminate stubborn field emitters through ion bombardment. Field emitted electrons ionize the gas resulting in localized sputtering of the emitter, and also suppressing field emission via ion implantation which serves to increase the local work function [28]. When radiation levels returned to background levels, the Kr gas was evacuated and the photogun returned to vacuum conditions and voltage was increased again. High voltage conditioning to −360 kV took approximately 70 hours including several soaking periods, with numerous field emission sites eliminated. The photogun

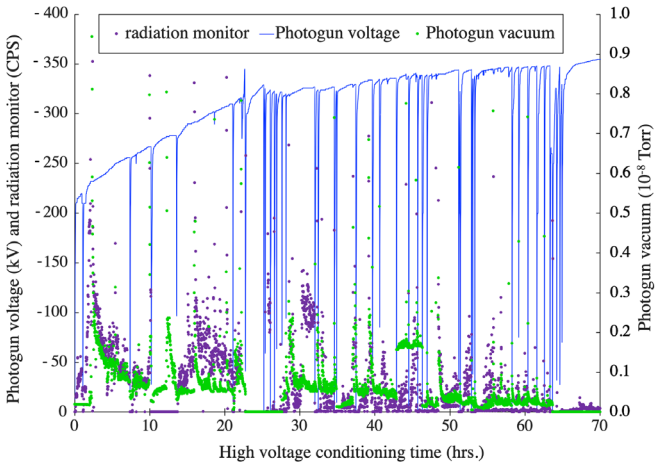

FIG. 2. History of photogun high voltage conditioning to −360 kV under UHV conditions and with krypton gas. Blue trace, voltage applied to the gun; green trace, the vacuum level as indicated by the ion pump; purple trace, x-ray radiation level from the Geiger monitors. During conditioning, radiation and vacuum levels diminish as field emitters were processed out, typically under Kr gas conditions, indicated by the vacuum level trace at 0 when the ion pump was turned off. Sharp vertical lines indicate the voltage tripping off, due to field emission current exceeding the current-limit setpoint of the high voltage power supply, set to ∼500 μA.

was deemed fully conditioned at −360 kV with radiation levels indistinguishable from background levels.

B. Photocathode activation vacuum chamber

Cs_xK_ySb photocathodes were manufactured in a vacuum chamber designed to accommodate up to five molybdenum pucks, where each puck supports one photocathode substrate. Pucks are cylindrical and cup shaped with a front face that accepts a 15 mm square substrate and a hollow back that accepts a heater and sample manipulator for puck movement. The photocathode activation vacuum chamber shown in Fig. 3 has four magnetically coupled sample manipulators: a long manipulator with translation and rotation capability for moving pucks into or out of the photogun, a short manipulator with translation and rotation capability for moving pucks from/onto the heaters and for transferring pucks to/from the long manipulator, and two short manipulators with only translation capability that serve as puck storage. The photocathode deposition chamber was equipped with two SAES WP1250 NEG modules, a 20 l/s ion pump, and a residual gas analyzer mass spectrometer (SRS model RGA200). A vacuum level on the order of 10^{-11} Torr was achieved following a 36 hr vacuum bake at 190 °C with a full activation of the NEG pumps at the end of the bake cycle.

Photocathodes were fabricated using a two-step sequential deposition technique similar to that described in Ref. [25]. The chemical sources were moved below the

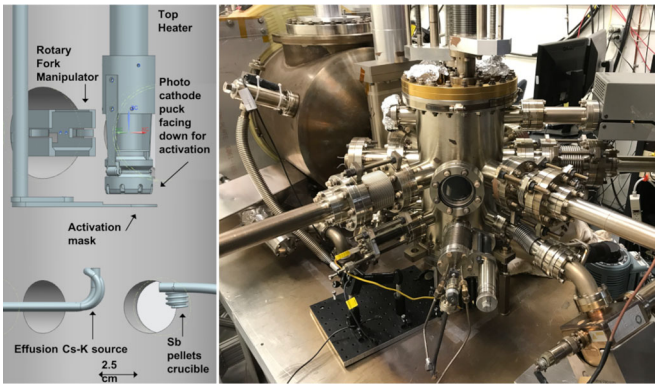

FIG. 3. Left: Diagram of the photocathode activation vacuum chamber internal components showing the photocathode puck facing down behind the mask for photocathode fabrication. Right: Photograph of the photocathode activation vacuum chamber. The photogun high voltage chamber can be seen in the foreground, with the gate valve separating the two vacuum chambers.

puck substrate, one source at a time. Antimony was deposited first from a heated crucible that holds Sb pellets held in place by gravity. The alkali metals cesium and potassium were deposited using an effusion source containing both species.

There are two heaters: one capable of reaching high temperature for boiling away residual chemicals on the substrate (i.e., substrate cleaning), and one for maintaining the substrate at an elevated temperature during photocathode fabrication. The heaters are inserted into the cup-shaped pucks using bellows linear-motion translation stages. For substrate cleaning, the puck faces up, and for photocathode fabrication the puck faces down. A 304L stainless-steel paddle with three holes (0.3, 0.5, and 0.7 cm diameter) can be rotated into position between the chemical sources and the substrate, to limit the dimensions of the photocathode and to position the photocathode active area off-axis relative to the photocathode center [21].

The following paragraphs describe the photocathode fabrication process in more detail. For most of the measurements described in this paper, a 600 micron-thick GaAs wafer with ⟨110⟩ cleave plane and p-doped with Zn ($\sim 1 \times 10^{19}$ cm^{-3}) served as the photocathode substrate. Photocathode films were also grown on 0.1 cm thick molybdenum substrates. The substrates were firmly attached to pucks using indium foil and a tantalum retaining ring crimped tightly to the edge of the puck. First, a puck was placed on the bottom heater with the substrate facing up and heat-cleaned at ∼450 °C for ∼8 hr. The indium foil melts during the heat cycle providing good thermal contact between the puck and the substrate. Upon cooling to room temperature, the puck was transferred to the top heater with the substrate now facing down and positioned above a heated ceramic crucible container holding the antimony pellets by gravity. The substrate must be maintained at an elevated temperature during photocathode fabrication. As

such, the top heater employs sapphire rollers attached to leaf springs that mate with a slot cut into the outer surface of the puck, to hold the puck securely in place and to provide good thermal contact to the heater surface. In addition, the top heater is attached to an electrically isolated bellows translation stage, to position the puck approximately 2 cm above the evaporation sources and 0.1 cm from the activation mask, and to bias the puck at −240 Volts Direct Current (VDC) during photocathode fabrication.

The top heater maintains the substrate temperature at ∼120 °C during deposition. Antimony was evaporated for 10 minutes by supplying 25 A to the tungsten heater coil wrapped around the crucible, and then retracted. Then the effusion source was positioned below the photocathode. The effusion source was heated using hot nitrogen gas passing through stainless-steel tubing brazed to the main Cs and K dispenser tube. A valve on the effusion source in combination with the nitrogen gas temperature were used to control the alkali source flow. Instead of a crystal thickness monitor, a residual gas analyzer served as a relative deposition monitor for the photocathode chemical species. The photocathode QE was continuously monitored during fabrication using a low-power 532 nm laser, with alkali species applied to the photocathode until QE stopped increasing achieving typical QE values in the range of 5% to 10% in about 100 minutes. Preliminary scanning electron microscopy in conjunction with energy dispersive X-ray spectroscopy analysis indicates photocathodes grown in the deposition chamber are cesium rich, with elemental composition $Cs_{0.75}K_{0.25}Sb$. Admittedly, the photocathode samples were exposed to air before installation in the SEM-EDS apparatus, resulting in a heavily oxidized surface, so the exact chemical composition of the photocathodes is not known at this point. A more detailed elemental composition analysis and characterization of various photocathode films will be presented in a future publication. Once a photocathode was fabricated, it was transferred to the photogun or stored on one of the short linear translation magnetically coupled sample manipulators.

C. Drive laser

A laser system composed of a gain-switched diode laser operating at wavelength 1.066 μm, followed by a multistage Yb-fiber amplifier chain and wavelength converter, was constructed for this project that provides light with rf structure at 533 nm and W of power. The laser system possesses features that are highly desirable for photocathode-based electron accelerator applications: adjustable pulse repetition rates from tens of MHz to a few GHz and direct synchronization to an external rf signal (i.e., the accelerator) without requiring complicated locking systems common to mode-locked drive lasers.

A schematic of the photogun drive laser system is shown in Fig. 4. The sub-mW light from the gain-switched diode

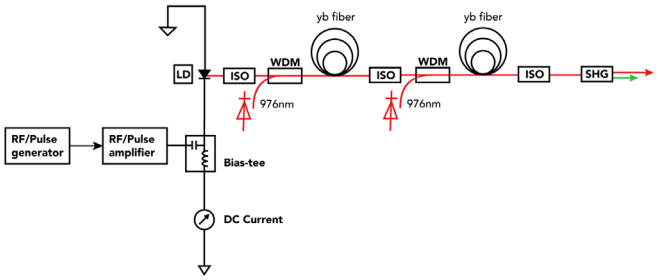

FIG. 4. Schematic of the rf-pulsed green-light driver laser system (LD, laser diode; ISO, optical isolator; WDM, wavelength division multiplexer; SHG, second harmonic generation crystal).

laser was amplified using two homebuilt Yb-doped fiber amplifiers. The first Yb-doped amplifier, or preamplifier, is a 4 m long Yb-gain fiber pumped with 976 nm light using a wavelength division multiplexer. The second fiber amplifier, or power amplifier, consists of a 5 m long highly doped double-clad Yb fiber with a 10 μm diameter core and 125 μm diameter cladding, a signal/pump combiner, a multimode 976 nm pump diode laser, and a stripper for separating the pump beam from the seed light. Optical isolators after each amplifier prevent retroreflections from returning to the amplifiers and bandpass filters after each amplifier were used to remove residual pump light and amplified spontaneous emission from the 1.066 μm output beam. All of the fibers are polarization maintaining which served to improve system stability. The light at 1.066 μm wavelength was then converted to 533 nm using a free-space periodically poled lithium niobate frequency doubling crystal. For the tests reported here, the laser operated at 374.25 MHz with 22 ps rms optical pulses. A more detailed description of the laser system will be presented in a future publication.

Light from the drive laser was delivered to the photogun approximately 5 m away via mirrors within a light-tight enclosure. The average power and laser pulse energy could be continuously varied using a rotating wave plate attenuator. Low duty-factor machine-safe electron beam was produced using an rubidium titanyl phosphate Pockells cell and a mechanic shutter (called tune-mode generator), where machine-safe refers to protection of the yttrium aluminum garnet (YAG) view screens and wire-scanner beam line diagnostics. The size of the laser beam incident on the photocathode was adjusted using a simple telescope lens system. A cylindrical lens was employed to ensure a circular laser profile at the photocathode illuminated at 25 degree angle of incidence (see Fig. 1). The laser linear polarization was oriented p-polarized with respect to the photocathode surface to enhance laser absorption within the photocathode. The transverse profile and size of the laser spot on the photocathode was measured and monitored by placing a beam splitter between the last lens and the viewport in the photogun high voltage vacuum chamber. The diverted laser beam was guided to a virtual photocathode composed of a CCD camera positioned at

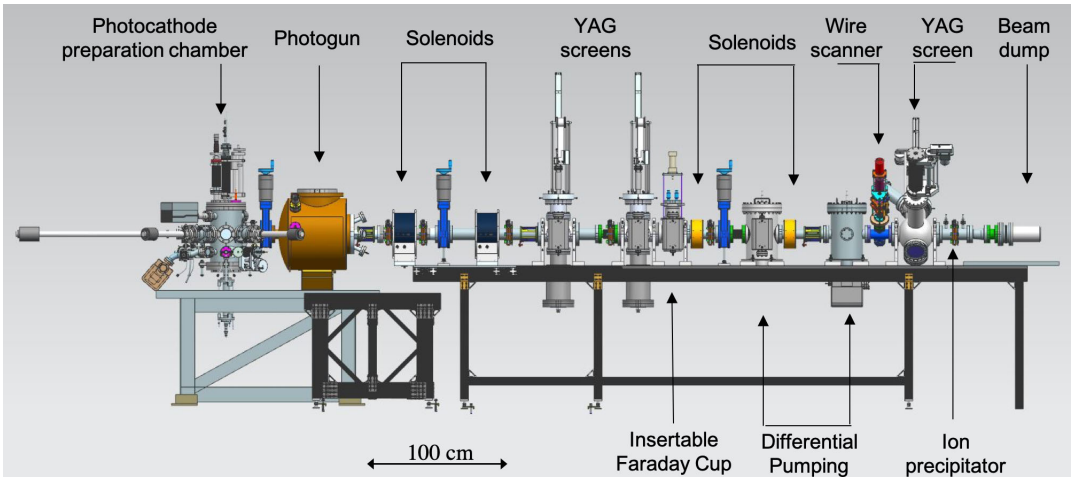

FIG. 5. Schematic of the photogun test stand and diagnostic beam line.

the same distance as that from the beam splitter to the photocathode. The image from the CCD camera was processed by Spiricon laser beam profiler software.

D. Diagnostic beam line

The photogun was connected to a 4-meter long diagnostic beam line with nominal 6.3 cm diameter aperture. Figure 5 shows a schematic of the beam line. A large-beampipe aperture was chosen to minimize beam loss expected from a large beam envelope during operation at high bunch charge and to manage beam halo at high average current. The strategy for the beam line vacuum design was based on differential pumping sections to vacuum isolate the gun from the beam dump where significant gas loads are expected during high current operations. Additionally, the beam dump was degassed to 400 °C prior to installation and an ion precipitator was mounted just upstream of the beam dump. The effect of ions in the beam line and mitigation techniques will be discussed in Sec. V. The beam line has three diagnostic vacuum crosses, each housing one SAES CapaciTorr MK5 NEG cartridge and one 40 l/s ion pump. Two differential pumping stations each consisting of four SAES WP1250 with ST707 material modules and a 40 l/s ion pump are positioned between the second and third diagnostic crosses. The beam line was vacuum baked to 200 °C for ∼72 hours. All of the NEG modules were activated just before the cool down to room temperature. All of the ion pumps are powered by an in-house power supply designed to measure sub-nA current levels [29]. This sensitive ion pump current monitor is beneficial to characterize vacuum conditions (after calibration against a vacuum gauge), and in particular serves as a diagnostic for beam loss. The baseline ion pump current in the beam line was 2 nanoamperes a few days after the vacuum bake, equivalent to $\sim 1 \times 10^{-11}$ Torr.

The electron beam optics design principle was based on providing a suitable envelope for transporting the beam to the dump with minimal loss. Focusing is provided by four hard-edge solenoids with ∼50 cm focal length each. There are beam waists at the photocathode, at the diagnostic crosses, and at the wire scanner with collimated beam in between the common solenoid pairs. Steering dipole pairs are positioned upstream of each solenoid and each diagnostic cross.

Each beam diagnostic cross has an insertable YAG crystal screen 100 μm thick and 5 cm diameter mounted to a thin aluminum frame attached to a shaft driven by a pneumatic air cylinder. The electron beam strikes the YAG screen at normal incidence producing a beam image which is then reflected off a mirror mounted at 45° behind the YAG screen. The image is delivered through a fused silica vacuum viewport to a CCD camera installed ∼100 cm from the 45° mirror, which is mounted ∼10 cm from the vacuum viewport. The YAG screen is imaged onto the CCD sensor with a 50 mm 1:1.8 lens attached to the camera. The resulting image is digitized with 0.12 mm/pixel resolution. When retracted for cw beam delivery, the YAG screens are replaced by a beam-shield tube matching beampipe diameter. The tube, originally designed for another application utilizing ps-long bunches where wakefield effects must be minimized, has longitudinal slots to provide some level of pumping. The third diagnostic cross located 50 cm upstream of the beam dump also includes a wire scanner consisting of a frame with a tensioned 20 micron-thick, 75% tungsten + 25% rhenium wire. The electron beam current was measured at low duty factor using an insertable Faraday cup located in the middle of the beam line, while high average beam current was measured with a water-cooled, electrically isolated beam dump.

III. ELECTROSTATIC DESIGN

The design of the photogun followed an iterative approach with respect to achieving desired mechanical, vacuum and high voltage features that sought to balance the

competing requirements for achieving reliable operation at −300 kV without field emission or high voltage breakdown, while still providing excellent beam properties and 10^{-12} Torr-scale vacuum. The following interconnected considerations influenced the design.

(a) No field emission, to provide long photocathode lifetime.—Field emission current strongly depends on the electric field strength which is determined by the applied voltage, cathode size and radius of curvature, anode/cathode gap and the distance to the vacuum chamber walls. Experience of several groups has shown field emission can be negligible (after high voltage conditioning) when gradient is maintained below ∼10 MV/m, assuming proper cleaning techniques were applied before and during assembly to minimize the amount of particulates inside the photogun vacuum chamber.

(b) No high voltage insulator breakdown (i.e., arcing).—This can be achieved using a screening electrode that reduces the field strength at the triple-point junction (ceramic-electrode-vacuum interface). The screening electrode also serves to linearize the potential across the length of the insulator.

(c) Symmetric radial electric field in the anode-cathode gap to minimize beam deflection.—Because the electrode-insulator assembly is not coaxial to the beam path, the radial electric field in the anode-cathode gap is asymmetric and the screening electrode can amplify this field asymmetry, which can result in a significant beam deflection at the exit of the photogun. Electrode dimensions were chosen to minimize this field asymmetry for minimal beam deflection at the design operating high voltage.

(d) Vacuum features.—An operating pressure in the 10^{-12} Torr range can be achieved by minimizing the surface area and outgassing rate of the photogun vacuum chamber and its internal components, and using standard NEG modules that surround a significant portion of the anode/cathode gap [11].

Field emission and high voltage breakdown are often the main limiting factors related to reliable dc high voltage photogun operation, at least when bias voltage exceeds ∼100 kV [10].

Electrostatic field maps are used to optimize electrode geometry and physical size per the aforementioned guidelines, but generating electrostatic field maps of noncylindrical geometries requires the use of sophisticated 3D modeling software. In this work, field maps were generated using the CST MicroWave Studio electrostatic solver [30]. Iterative adjustments to the electrostatic model served to optimize the diameter of the cathode electrode within the gun chamber, set the cathode-anode gap, and to refine the shape of the triple-point-junction screening electrode with the overall goal of keeping the electric field strength less than ∼10 MV/m at −350 kV bias voltage. This led to a cathode-anode spacing of 9 cm and the contour of the screening electrode shown in Fig. 6. These electrostatic field maps were then used in particle tracking code simulations to verify that the chosen geometry provided adequate beam transport for beam at current up to ∼5 mA and bunch charge <20 pC. The Pierce focusing angle of 25° and the hole diameters of the cathode and anode electrodes were identical to those used at CEBAF. The following considerations were applied to the design of the triple-point junction screening electrode.

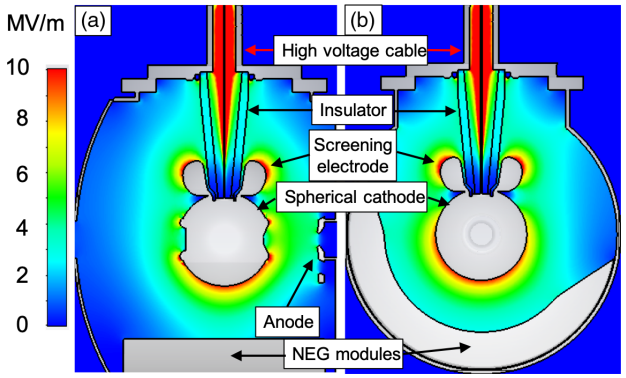

FIG. 6. Electrostatic model of the photogun at −300 kV. The color represents the electric field strength in MV/m. (a) Side view cross section with the anode-cathode gap on the right. (b) Front view cross section looking from the anode. The NEG modules that line the bottom of the vacuum chamber could not be installed symmetrically due to the position of their electrical feedthrough.

(a) The distance between the insulator surface and the screening electrode and its contour near the triple-point junction were adjusted to minimize the electric field strength both parallel and perpendicular to the surface of the insulator. Field-emitted electrons from the triple-point junction can initiate prebreakdown currents that often lead to arcing along the ceramic insulator at the cable-plug interface.

(b) The height and radius at its cusp were adjusted to minimize the electric field at the triple-point junction while keeping the contour field strength less than 10 MV/m at −350 kV. The height of the screening electrode influences the potential along the insulator, especially at the interface between the insulator- and the high-voltage plug. A taller screening electrode creates a more linear change in the potential, but it will increase the field strength at its cusp because it has moved closer to the grounded vacuum chamber wall.

(c) The outermost radius was adjusted to maintain a radius smaller than the spherical electrode radius, in order to minimize distortions to the electric field in the anode-cathode gap.

The net result of the screening-electrode modeling was to reduce the electric field strength parallel to the insulator axis at the high voltage triple-point junction from ∼2.7 MV/m (no screening electrode) to about 0.2 MV/m (Fig. 7). Beyond the triple-point junction (distance > 5 cm), the

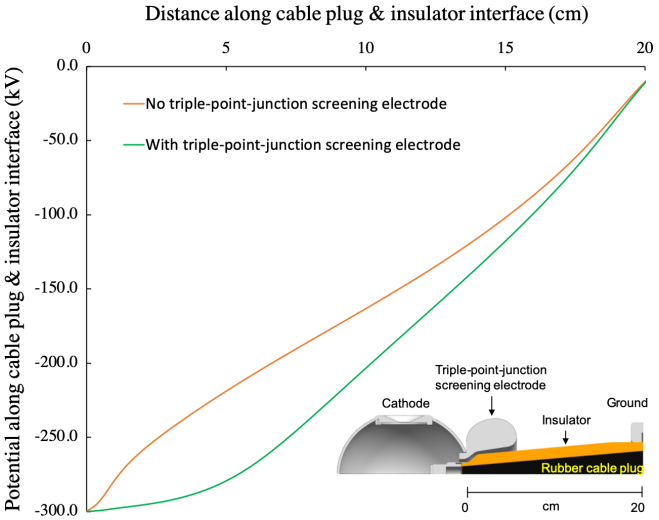

FIG. 7. Electrostatic potential along the interface between the high-voltage-rubber cable plug and the ceramic insulator for cathode electrode biased at −300 kV. The inset shows a model of the assembly.

screening electrode design served to linearize the potential drop along the length of the insulator.

For electron beams produced off-axis in photoguns with focusing electrodes, the nonzero transverse fields within the anode-cathode gap deflects the electron beam as it leaves the photogun. Our photogun design, although providing practical benefits related to photocathode replacement and reliable high voltage operation, introduced an asymmetry in the transverse electric field within the anode-cathode gap that enhanced the typical beam deflection observed from photoguns with completely symmetric high voltage designs. With the laser beam positioned in the center of the photocathode, and with the cathode electrode biased at −300 kV, a vertical beam deflection of 1.5 cm was observed at the first beam line solenoid lens located 50 cm downstream of the photocathode. The asymmetry in the vertical electric field is illustrated in Fig. 8(a) where the color map (top graph) shows the E_y distribution within the anode-cathode gap, and the bottom graph shows the magnitude of E_y along each of the colored dotted lines shown on the field map. The vertical position of each dotted line is indicated with respect to the axis (black line, $y = 0$) for which the E_y should be zero, but due to the photogun geometry, it is nonzero throughout the anode-cathode gap indicating that the observed vertical beam deflection is indeed due to the vertical field asymmetry. Although this effect was most pronounced in the vertical plane, there is a similar asymmetry in the horizontal electric field throughout the anode-cathode gap shown in Fig. 8(b), which stems from the asymmetric installation of NEG modules (Fig. 6) and ground screen.

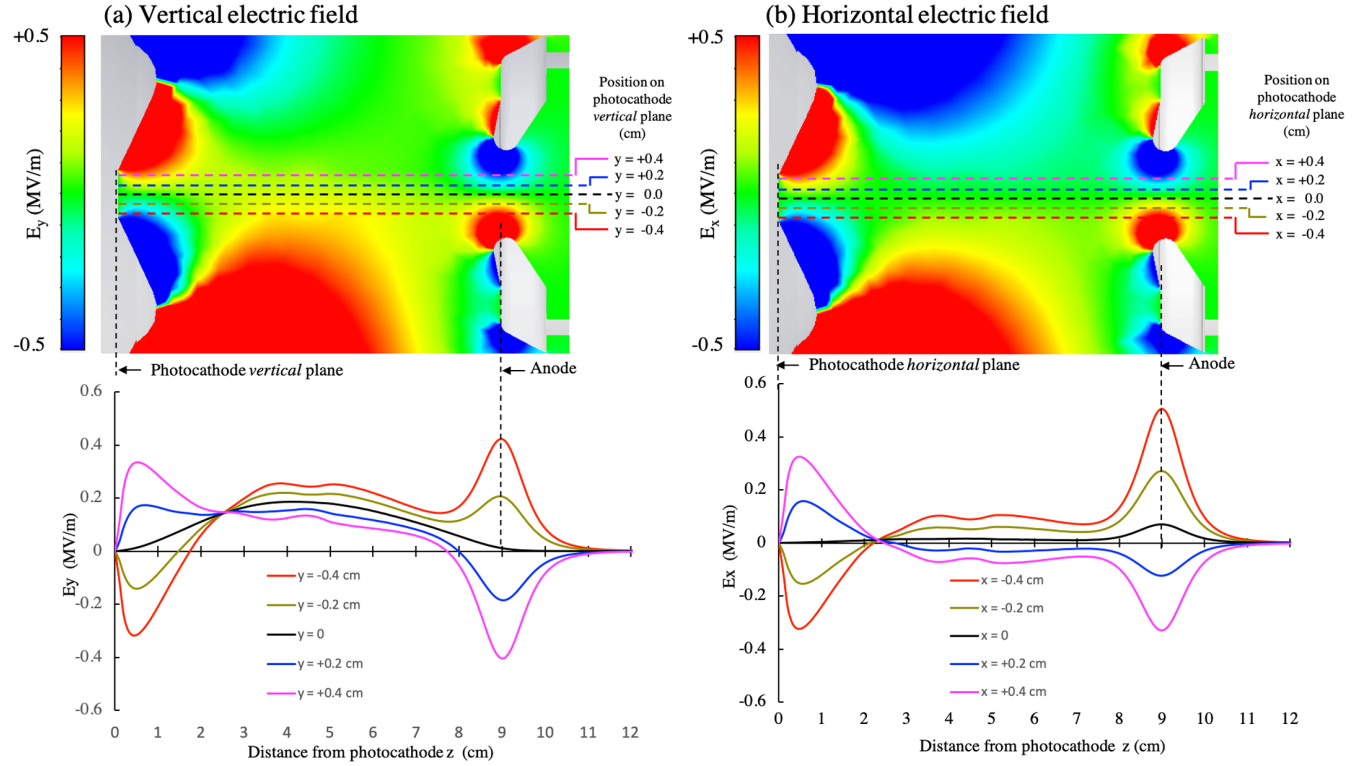

FIG. 8. Color map of the photogun anode-cathode gap at −300 kV showing the transverse electric field Ey within the anode-cathode gap, in a vertical plane centered on the anode-cathode axis (a). The bottom plot shows the magnitude of Ey plotted along the dotted lines shown in the field map. The position of each dotted line is indicated with respect to the axis, and (b) corresponding plots for Ex.

IV. EMITTANCE MEASUREMENTS

Emittance measurements were frequently made using both diagnostics—YAG screens and the wire scanner—to cross compare and validate results. Beam emittance was first measured as a function of average current to find beam conditions without significant space charge effects, but at currents sufficiently high to be resolved by the wire scanner electronics. This was achieved by adjusting the drive laser power and macropulse time structure to 250 μs long pulses at 1.5% duty factor to generate ∼100 nA average current resulting in ∼20 femto-Coulombs bunch charge. Next, the beam emittance was measured as a function of gun bias voltage to validate that normalized emittance values were constant. It was noted that the signal from the wire scanner was nearly indistinguishable from background with the photogun biased at −300 kV. At lower beam energies, the net number of electrons stopped by the wire generate a negative signal. At higher energies, the net number of secondary electrons knocked out from the wire generate a positive signal. Around 300 keV, it turns out that the signal is very small. So although the photogun operated reliably at −300 kV, the emittance measurements described below were performed at −200 kV bias voltage.

The emittance was measured across the photocathode vertical and horizontal axes with the single-solenoid scan method, imaging the electron beam on a YAG screen 300 cm downstream of the first solenoid with an average beam current of a few nA. Figure 9 shows the vertical and horizontal emittances measured at several positions along the photocathode vertical and horizontal axes up to a radius of 0.2 cm. Beyond this radius, the focusing electrode produced very astigmatic beam, making emittance measurements very difficult beyond the central region of the photocathode. The normalized rms emittance from the photocathode center was 0.09 ± 0.01 mm mrad with 0.2 mm rms laser spot size. The results shown in Fig. 9 suggest an asymmetry in the vertical emittance along the vertical axis of the photocathode, likely due to the asymmetric electrostatic nature of the anode-cathode geometry as shown in Fig. 8. A similar effect but less prominent can be seen in the horizontal emittance along the horizontal axis of the photocathode, as a result of the asymmetric placement of NEG pump modules and ground screen.

The experimental results shown in Fig. 9 were obtained using YAG screen images for a set of solenoid current values. To determine x, y rms beam sizes, beam images were first captured on the YAG screen with an in-house video frame-grabber software that was also used to rotate each beam image by the Larmor angle to account for the coupling between the x,y transverse planes incurred by the solenoid magnet [31]. The solenoid scan formalism in Ref. [32] was then implemented to characterize x^2_{rms} and y^2_{rms} from the projected x, y rms beam sizes vs solenoid current. The transfer matrix of the solenoid scan beam line without aberrations is expressed as $R = R_d R_{\mathrm{foc}}$, where R_d

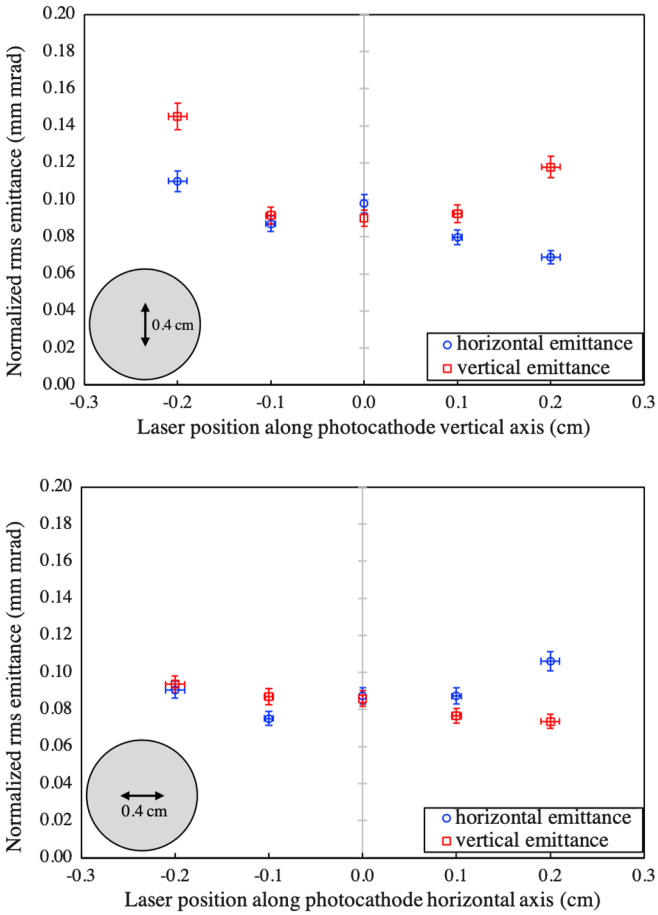

FIG. 9. Normalized rms emittance measured for a set of laser positions along the vertical axis (top) and horizontal (bottom) axis of the photocathode. The laser spot size at the photocathode was 0.2 mm rms and the photogun voltage −200 kV. The inset in each graph depicts the size and orientation of the laser scan with respect to the photocathode.

is the drift matrix and R_{foc} is the focusing matrix. A rotation matrix was not employed in the calculation because the beam images were rotated by the Larmor angle using the video "frame-grabber" software. Equation (15) in Ref. [32] shows the analytical expression for the expected x-beam sizes squared as

$$x^2_{\mathrm{rms}} = (C - L_d K S)^2 \langle x^2 \rangle + 2(C - L_d K S) \cdot (S/K + C L_d) \langle x x' \rangle + (S/K + C L_d)^2 \langle x x'^2 \rangle, \quad (1)$$

where $\langle x^2 \rangle$, $\langle x' \rangle$, and $\langle x'^2 \rangle$ are the beam moments at the solenoid entrance, and K ($\frac{eB_0}{2\beta\gamma mc}$), L and B_0 are the strength, effective length and the peak magnetic field of the solenoid respectively, L_d is the length of the drift, $C = \cos(KL)$, and $S = \sin(KL)$. To provide confidence in the experimental results and subsequent implementation of the solenoid scan formalism, the particle tracking code Elegant was utilized to calculate x_{rms} and y_{rms} from a 10 000 particle

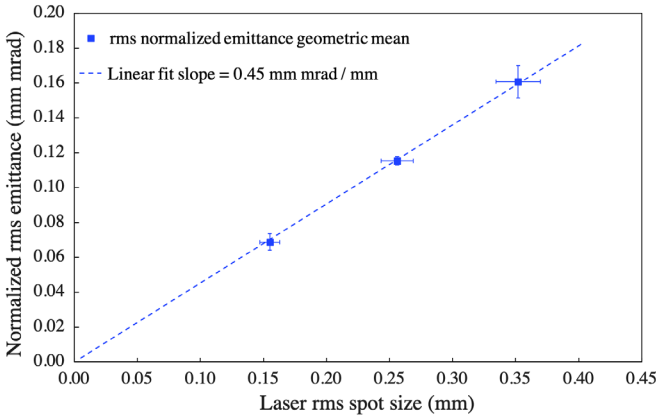

FIG. 10. Normalized rms emittance vs laser rms spot size at the photocathode for laser wavelength 533 nm. From the linear curve fit slope, the thermal emittance is 0.45 ± 0.02 mm mrad/mm.

distribution defined by the Twiss analysis resulting from the curve fitting of Eq. (1) for a solenoid scan. From the Elegant results, x^2_{rms} and y^2_{rms} vs solenoid current were calculated and compared to the measured values, showing good agreement.

After assessing the emittance across the face of the photocathode, the single-solenoid scan was implemented to measure the photocathode thermal emittance. The laser beam was positioned at the center of the photocathode and it was found that the electron beam transverse profile was circular at the wire scanner. In this manner, the Larmor rotation angle introduced by the solenoid was ignored in the formalism used to calculate the vertical and horizontal emittances. Figure 10 shows the results of the normalized rms emittance geometric mean $\epsilon_n = \sqrt{\epsilon_x \epsilon_y}$ measured as a function of laser spot size using 20 femto-Coulombs bunch charge. The slope of the curve fit in Fig. 10 indicates that the obtained thermal emittance was 0.45 ± 0.02 mm mrad/mm.

The mean transverse energy (MTE) is a figure of merit used to characterize the photocathode thermal emittance, obtained from the slope of normalized rms transverse emittance (ϵ_n) as a function of the rms laser spot size σ [31]. The normalized rms transverse emittance at the cathode is given by

$$\epsilon_n = \sigma \sqrt{\frac{\mathrm{MTE}}{m_0 c^2}}, \tag{2}$$

where m_0 is the electron rest mass and c is the speed of light.

From the slope shown in Fig. 10 and using Eq. (2), we obtain MTE $= 105 \pm 10$ meV. For a simple photoemission model, the theoretical MTE is defined as [31]

$$\mathrm{MTE} = \frac{h\nu - (E_g + E_a)}{3}, \tag{3}$$

where E_g is the energy gap, E_a is the electron affinity and $h\nu$ is the photon energy. Using $E_g = 1.0$ eV and $E_a = 1.1$ eV for CsK_2Sb as listed in Table 3 of Ref. [33] and for $h\nu = 2.326$ eV, MTE $= 75$ meV, while MTE $= 142$ meV in Ref. [31] with $E_g = 1.2$ eV, $E_a = 0.7$ eV and $h\nu = 2.326$ eV. Our MTE result is between these values as it is likely that our photocathodes have different stoichiometry than those studied by other groups. We have not measured the energy gap nor the electron affinity of our photocathodes.

V. ION PRODUCTION AND ITS EFFECT ON PHOTOCATHODE LIFETIME

Initial attempts to generate sustained milliampere beam were unsuccessful, hindered by intermittent but frequent stepwise QE loss. An example is depicted in Fig. 11 which shows the high voltage power supply current, the beam dump current, and the gun ion pump current/vacuum pressure as a function of time during an attempt to deliver 1 mA beam. With the drive laser power kept constant, the power supply current and beam current slowly increased during the first minutes of beam delivery, but soon sharp drops in QE were observed accompanied by high voltage power supply current spikes and vacuum bursts detected by the photogun and beam line ion pumps. During other runs, the power supply would sometimes trip off with current spikes exceeding 5 mA which was the maximum current the power supply could provide. Operating under these conditions, damage sites were clearly visible on the photocathode: a picture of one of the damaged photocathodes is shown in the inset of Fig. 11. Incidents like this and characterized by current surges from the photogun high voltage power supply were termed micro-arc discharges.

Sustained high current beam delivery was eventually achieved by applying a positive bias (+1000 VDC) to the

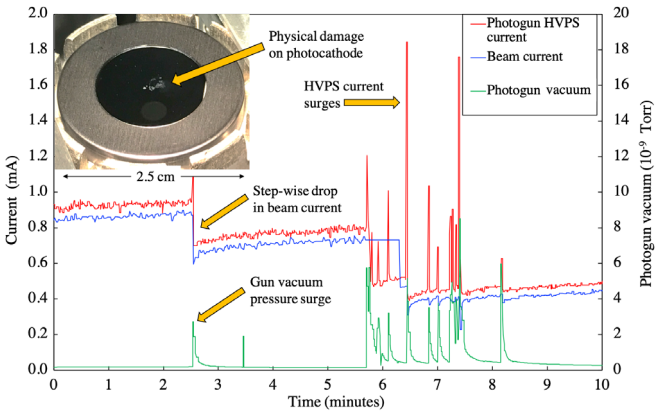

FIG. 11. Photogun high voltage power supply current (HVPS), beam dump current and photogun vacuum during one of the initial 1 mA demonstration attempts. Each sharp decrease in beam current (blue) is associated with high voltage power supply current (red) and pressure (green) spikes that leave craterlike markings on the photocathode surface (inset).

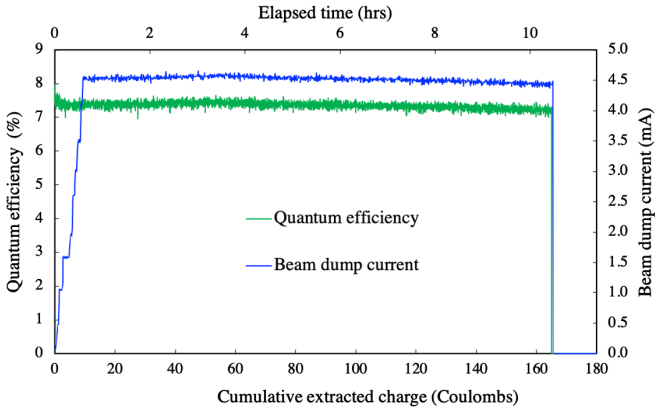

FIG. 12. Photocathode QE measured over 10 hours with the photogun biased at −300 kV and delivering 4.5 mA average current. The 1/e QE charge lifetime was ∼6600 C. The anode was biased at +1000 VDC, and the beam line ion precipitator at −200 VDC. The drive laser was operating at 374 MHz with 22 ps pulses rms producing 12 pC bunch charge. The laser spot size at the photocathode was 0.04 cm rms positioned off center 0.25 cm, on Cs_xK_ySb photocathode with 0.5 cm diameter active area.

anode [26,34,35]. Figure 12 shows beam current delivered to the beam dump at 4.5 mA cw, the effective hardware limit of the high voltage power supply, sustained over a 10-hour long test run with the photogun biased at −300 kV. Although the photogun high voltage power supply could provide a maximum current of 5 mA, for photocathode lifetime tests the maximum current from the photogun was set to 4.5 mA because noise on power supply current readback would sometimes exceed the 5 mA limit and the gun high voltage power supply would trip off. The 1/e quantum efficiency lifetime was over 6600 Coulombs with the quantum efficiency remaining nearly constant after delivering 160 Coulombs. The photogun vacuum level increased from 7×10^{-12} Torr baseline to 2×10^{-11} Torr at 4.5 mA cw and remained at that level for the duration of the run, which was terminated to give way for other tests. When photocathodes grown on molybdenum substrates were tested, the photocathode lifetime was even better, with no measurable QE decay.

Beam line ion precipitator electrodes (see Fig. 5) similar to those described in Ref. [36] were also tested as a means to preserve photocathode QE, but alone (i.e., without the biased anode), these ion-clearing electrodes did not prevent rapid QE loss and photocathode damage, although the damage threshold beam current increased from 1 to 3 mA. Significantly improved lifetime was largely attributed to the biased anode.

It must be mentioned that during past work using a different test stand with a photogun operating at −200 kV and with an alkali-antimonide photocathode [37], the biased anode provided no measurable benefit. Photocathode lifetime was the same with anode biased or grounded. In light of present work, it is quite likely this stems from the markedly better vacuum conditions of the −200 kV photogun and test beam line, originally used for spin-polarized electron beam tests using GaAs photocathodes. The −200 kV photogun test beam line includes NEG-coated beampipe and a 15° bend that would serve to restrict downstream beam line ions from reaching the photogun. But it must also be pointed out that under some run conditions that were explored during previous tests (namely, when using a diode drive laser operating at 405 nm with relatively poor laser spatial mode quality, and with the laser spot located at the very edge of the photocathode where beam transport conditions are suboptimal), similar stepwise drops in QE were observed but they were attributed to static charge buildup on beam line ceramic view screens that were in direct line of sight of the beam. At the time, it was hypothesized that charging and discharging of view screens could change the beam orbit, with temporarily mis-steered beam at the Faraday cup beam dump suggesting an apparent QE reduction. However in light of new work reported here, this hypothesis now appears to be incorrect. In fact, micro-arc discharges were present during previous tests too, however during these tests the discharges were not so problematic, with QE fully recovering and even improving throughout beam delivery, likely a result of better vacuum conditions.

To better understand the remarkable lifetime improvement observed using the biased anode, the anode-cathode gap and a portion of the adjacent beam line were modeled using the ion beam simulator code, IBSIMU [38], which is a powerful suite of libraries based on C++ programming language for low-energy particle tracking in electric and magnetic fields. The open source distribution code has been utilized in the design of ion sources [39,40]. IBSIMU is designed for unbunched (dc) beams only. Its main distinction from particle in cell tracking codes like ASTRA [41] (commonly used for modeling space charge dominated, bunched electron beam dynamics) is that it generates and tracks ions produced by collisions of the main electron beam with residual gas, and subsequently generates and tracks secondary electrons and ions. One of the libraries uses a Monte Carlo generator to generate randomly the primary ions along the trajectory of the primary electron beam, taking into account the mean-free path of the ionized residual gas. The primary ions are confined (and oscillate) in the potential well of the primary electron beam. The mean-free path calculation is based on the ionization cross section for hydrogen assuming a constant gas density (hydrogen is the dominant gas species within the photogun and beam line). The initial energy of the primary ions (less than 1 eV) was given random direction of motion. The electrostatic field distribution (2D, axisymmetric) of the photogun cathode electrode biased at −300 kV dc and the anode biased at +1000 VDC were generated using the electrostatic solver POISSON SuperFish [42]. The generated field maps were then exported to IBSIMU. The code then calculated the potential distribution ϕ by solving the Laplace equation

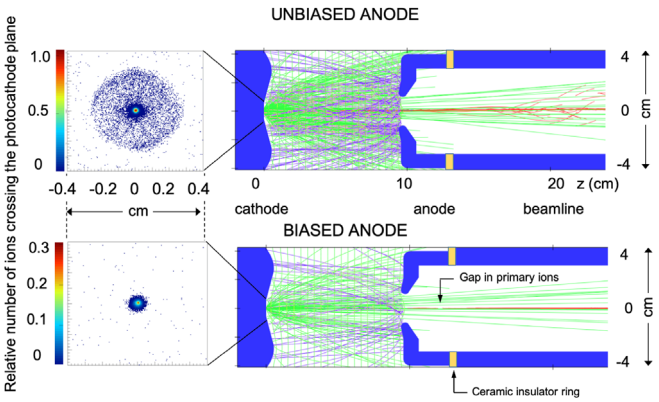

FIG. 13. IBSIMU simulation of the anode-cathode gap with the cathode electrode biased at −300 kV for two cases: Top: unbiased anode, and bottom: anode biased at +1000 VDC. The left shows the relative number of ions and their x/y position on the photocathode plane. The right shows the trajectories of primary ions (red traces) generated by the main electron beam (not shown), secondary electrons (green traces) and secondary ions (purple traces).

$\nabla^2\phi = 0$ on a mesh including the boundary conditions given by the biased anode and cathode electrodes and beam pipe. The charged particles created by the electron beam colliding with residual gas in the anode-cathode gap and the beam line are tracked through this electrostatic potential field. Details of the algorithm are given in Ref. [39].

IBSIMU simulation results are shown in Fig. 13, for electron beam produced from the center of the photocathode and for the anode unbiased, i.e., at ground potential (top). On the right side of Fig. 13, the trajectories of the primary ions shown as red traces are generated by the main electron beam (not shown) as it collides with residual hydrogen gas in the beam line. Secondary electrons (green traces) are generated by surface collision when the primary ions bombard the photocathode. Finally secondary ions (purple traces) are generated by surface collision when the secondary electrons strike the anode. When a positive bias of +1000 VDC was applied to the anode (Fig. 13, bottom), the simulation results show that the number of primary and secondary ions in the anode-cathode gap is significantly reduced (fewer red and purple traces), resulting in lower density of ions in the anode-cathode gap compared to the unbiased anode case. Looking closely at Fig. 13 (bottom), one can see a gap in the ion beam trajectories, a region in z free of ions in the vicinity of the anode support structure which was also biased at +1000 VDC.

The left side of Fig. 13 shows the relative number of ions and their x,y position on the photocathode plane. When the anode is unbiased, ions impact the photocathode over a circular region 0.6 cm in diameter. The total number of ions in the simulation was normalized to 1 for illustration purposes. In contrast, when the anode was biased to +1000 VDC, the size of the ion impact region at the photocathode was reduced to about 0.1 cm diameter and

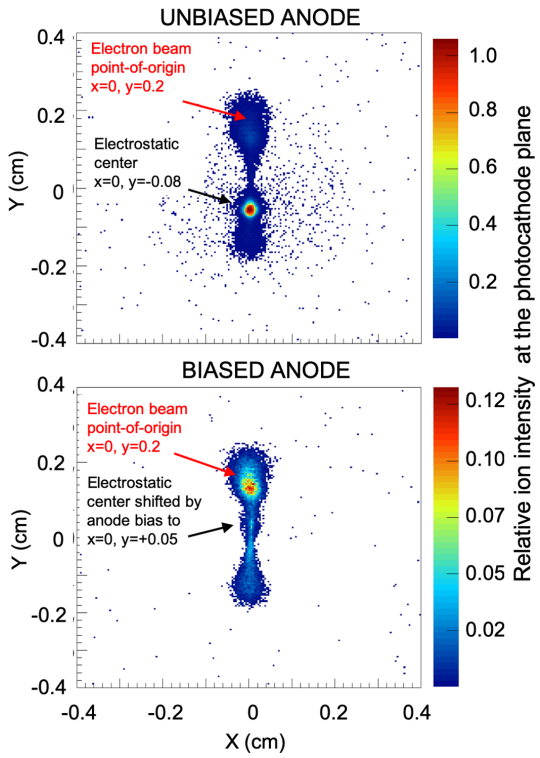

FIG. 14. IBSIMU results showing the number of primary ions impacting the photocathode for two conditions: unbiased anode (top) and anode biased at +1000 VDC (bottom). In both cases, the electron beam was extracted 0.2 cm above the photocathode center.

although the core of the ion beam striking the photocathode is similar in size to the unbiased anode case, the relative number of ions impacting the photocathode center decreased by 70%.

IBSIMU was also used to study off-axis beam production from the photocathode. Off-axis beam production is known to improve photogun operating lifetime, at least for GaAs photocathodes [1]. The simulation results in Fig. 14 show the relative intensity of ions and their position at the photocathode for a 300 keV electron beam generated 0.2 cm off axis for two cases, unbiased anode (top) and anode biased to +1000 VDC (bottom). The relative intensity of ions was normalized to 1 for the unbiased anode case, with the highest ion impact intensity observed at the electrostatic center ($x = 0$, $y = 0$) and distributed along a trench to the electron beam emission site ($x = 0$, $y = 0.2$ cm). This behavior is a result of the astigmatic nature of the Pierce-type electrode, with the photoemitted electrons following a curved trajectory toward the anode, creating ions along the way. The ions produced by the electron beam are accelerated to the negatively biased photocathode but experience little transverse deflection because of their comparatively large mass, forming the channel between the electrostatic center and the position where the electrons are emitted. Interestingly, the QE

trench extends beyond the electrostatic center, suggesting that the 25° Pierce-type electrode overfocuses the electron beam, i.e., the electron beam leaves the photocathode and crosses over the axis of the anode-cathode gap before leaving the photogun. This trenchlike distribution of ions at the photocathode plane shown in Fig. 14 closely resembles photocathode quantum efficiency maps presented in Ref. [1].

The bottom image of Fig. 14 once again illustrates the efficacy of minimizing ion bombardment of the photocathode using a biased anode. With the anode biased at +1000 VDC, the total number of ions striking the photocathode was reduced by ∼90%, and with most ions striking the photocathode near the electron beam point of origin.

VI. CONCLUSIONS AND OUTLOOK

A compact dc high voltage photogun was designed, built and operated reliably for over 1000 cumulative hours at −300 kV bias voltage with alkali-antimonide photocathodes. This is the highest bias voltage ever achieved with an inverted-insulator design that offers numerous practical advantages over designs that employ large cylindrical insulators. The key to achieving the desired bias voltage without high voltage breakdown was the cathode screening electrode which served to reduce the field strength at the triple-point junction and to linearize the potential across the insulator. Although the asymmetrical nature of the photogun design results in nonsymmetric radial electric field along the anode-cathode gap, the cathode electrode design did not adversely affect beam quality providing uniform transverse beam profile from the photocathode center. The measured thermal emittance from the Cs_xK_ySb photocathode was 0.45 mm mrad/mm at 533 nm, a value comparable to those reported by other groups [31,33].

Initial attempts to generate high current beam were hindered by overcurrent photogun power supply faults that resulted in stepwise QE decays and physical damage to the photocathode limiting beam production to about 1 mA. Biasing the anode was essential to overcome this problem and allowed sustained beam delivery at 4.5 mA. Ion-tracking Monte Carlo based simulations were presented to explain and quantify the benefits of the biased anode in terms of preventing beam line ions from entering the anode-cathode gap thus reducing ion bombardment of the photocathode. Our observations and simulations suggest that in sufficient density, ions within the anode-cathode gap may provide an arc path to ground, causing the observed micro-arc discharges that led to photocathode damage. Although alkali-antimonide photocathodes are certainly more rugged than sensitive GaAs-based photocathodes, our work suggests that ultrahigh vacuum conditions are needed in the anode-cathode gap to prevent ion-induced micro-arc discharges that limit high current beam production.

On-going studies will address the limitations of the electrostatic design, with the goal of reaching higher operating voltages, increased gradient at the photocathode and symmetrical radial field to produce bright beams at nano-Coulomb bunch charge. Beyond the performance described here, the photogun was used to generate magnetized electron beam at considerably higher current without measurable QE decay from Cs_xK_ySb photocathodes grown on molybdenum, an achievement that will be described in subsequent publications.

ACKNOWLEDGMENTS

This material is based upon work supported by the U.S. Department of Energy, Office of Science, Office of Nuclear Physics under Contract No. DE-AC05-06OR23177, and by the Laboratory Directed Research and Development funding.

[1] C. K. Sinclair, P. A. Adderley, B. M. Dunham, J. C. Hansknecht, P. Hartmann, M. Poelker, J. S. Price, P. M. Rutt, W. J. Schneider, and M. Steigerwald, Development of a high average current polarized electron source with long cathode operational lifetime, Phys. Rev. ST Accel. Beams **10**, 023501 (2007).

[2] R. Barday and K. Aulenbacher, Polarized electron source operation at average currents of several milliamperes, AIP Conf. Proc. **915**, 1019 (2007).

[3] G. Neil *et al.*, The JLab high power ERL light source, Nucl. Instrum. Methods Phys. Res., Sect. A **557**, 9 (2006).

[4] E. J. Minehara, Development and operation of the JAERI superconducting energy recovery linacs, Nucl. Instrum. Methods Phys. Res., Sect. A **557**, 16 (2006).

[5] D. Trbojevic *et al.*, CBETA—Cornell University Brookhaven National Laboratory Electron Energy Recovery Test Accelerator, in *Proceedings of the International Particle Accelerator Conference (IPAC'17), Copenhagen, Denmark, 2017*, International Particle Accelerator Conference No. 8 (JACoW, Geneva, Switzerland, 2017), pp. 1285–1289.

[6] A. V. Fedotov, Bunched beam electron cooling for the low energy RHIC operation, ICFA Beam Dyn. Newslett. **65**, 22 (2014).

[7] D. Kayran *et al.*, LEReC photocathode dc gun beam test results, in *Proceedings of the International Particle Accelerator Conference (IPAC'18), Vancouver, BC, Canada, 2018*, International Particle Accelerator Conference No. 9 (JACoW Publishing, Geneva, Switzerland, 2018), pp. 1306–1308.

[8] L. Cultrera, Cathodes for photoemission guns, in *Proceedings of the 24th Particle Accelerator Conference, PAC-2011, New York, 2011* (IEEE, New York, 2011), Vol. C110328, pp. 2099–2103.

[9] R. Forbes, J. Deane, A. Fischer, and M. Mousa, Fowler-Nordheim plot analysis: A progress report, Jordan J. Phys. **8**, 125 (2015).

[10] W. T. Diamond, New perspectives in vacuum high voltage insulation. I. The transition to field emission, J. Vac. Sci. Technol. A **16**, 707 (1998).

[11] M. Stutzman, P. Adderley, J. Brittian, J. Clark, J. Grames, J. Hansknecht, G. Myneni, and M. Poelker, Characterization of the CEBAF 100 kV dc GaAs photoelectron gun vacuum system, Nucl. Instrum. Methods Phys. Res., Sect. A **574**, 213 (2007).

[12] C. HernandezGarcia, S. V. Benson, G. Biallas, D. Bullard, P. Evtushenko, K. Jordan, M. Klopf, D. Sexton, C. Tennant, R. Walker, and G. Williams, DC high voltage conditioning of photoemission guns at Jefferson Lab FEL, AIP Conf. Proc. **1149**, 1071 (2009).

[13] N. Nishimori, R. Nagai, S. Matsuba, R. Hajima, M. Yamamoto, Y. Honda, T. Miyajima, H. Iijima, M. Kuriki, and M. Kuwahara, Experimental investigation of an optimum configuration for a high-voltage photoemission gun for operation at ≥ 500 kV, Phys. Rev. ST Accel. Beams **17**, 053401 (2014).

[14] J. Maxson, I. Bazarov, B. Dunham, J. Dobbins, X. Liu, and K. Smolenski, Design, conditioning, and performance of a high voltage, high brightness dc photoelectron gun with variable gap, Rev. Sci. Instrum. **85**, 093306 (2014).

[15] C. Hernandez-Garcia, T. Siggins, S. Benson, D. Bullard, H. F. Dylla, K. Jordan, C. Murray, G. R. Neil, M. Shinn, and R. Walker, A high average current dc GaAs photocathode gun for ERLs and FELs, in *Proceedings of the 21st Particle Accelerator Conference, Knoxville, TN, 2005* (IEEE, Piscataway, NJ, 2005), pp. 3117–3119.

[16] S. Benson *et al.*, High power operation of the JLab IR FEL driver accelerator, in *Proceedings of the 22nd Particle Accelerator Conference, PAC-2007, Albuquerque, NM* (IEEE, New York, 2007), pp. 79–81.

[17] B. Dunham *et al.*, Record high-average current from a high-brightness photoinjector, Appl. Phys. Lett. **102**, 034105 (2013).

[18] N. Nishimori, R. Nagai, R. Hajima, M. Yamamoto, Y. Honda, T. Miyajima, and T. Uchiyama, Operational experience of a 500 kV photoemission gun, Phys. Rev. Accel. Beams **22**, 053402 (2019).

[19] S. Benson *et al.*, Development of a bunched beam electron cooler based on ERL and circulator ring technology for the Jefferson Lab Electron-Ion Collider, in *Proceedings of the International Workshop on Beam Cooling and Related Topics (COOL'17): Bonn, Germany, 2017* (JACoW Publishing, Geneva, Switzerland, 2018).

[20] P. A. Adderley, J. Clark, J. Grames, J. Hansknecht, K. Surles-Law, D. Machie, M. Poelker, M. L. Stutzman, and R. Suleiman, Load-locked dc high voltage GaAs photogun with an inverted-geometry ceramic insulator, Phys. Rev. ST Accel. Beams **13**, 010101 (2010).

[21] P. A. Adderley, M. BastaniNejad, J. Clark, J. Grames, J. Hansknecht, J. McCarter, M. Poelker, M. L. Stutzman, R. Suleiman, and K. Surles-Law, CEBAF 200 kV inverted electron gun, in *Proceedings of the 24th Particle Accelerator Conference, PAC-2011, New York, 2011* (IEEE, New York, 2011).

[22] C. Hernandez-Garcia, M. Poelker, and J. Hansknecht, High voltage studies of inverted-geometry ceramic insulators for a 350 kV dc polarized electron gun, IEEE Trans. Dielectrics Electrical Insul. **23**, 418 (2016).

[23] C. Hernandez-Garcia, D. Bullard, F. Hannon, Y. Wang, and M. Poelker, High voltage performance of a dc photoemission electron gun with centrifugal barrel-polished electrodes, Rev. Sci. Instrum. **88**, 093303 (2017).

[24] M. A. A. Mamun, A. A. Elmustafa, C. Hernandez-Garcia, R. Mammei, and M. Poelker, Effect of Sb thickness on the performance of bialkali-antimonide photocathodes, J. Vac. Sci. Technol. A **34**, 021509 (2016).

[25] M. A. Mamun, M. R. Hernandez-Flores, E. Morales, C. Hernandez-Garcia, and M. Poelker, Temperature dependence of alkali-antimonide photocathodes: Evaluation at cryogenic temperatures, Phys. Rev. Accel. Beams **20**, 103403 (2017).

[26] J. Grames, P. Adderley, J. Brittian, J. Clark, J. Hansknecht, D. Machie, M. Poelker, M. Stutzman, K. Surles-Law, and E. Pozdeyev, A biased anode to suppress ion back-bombardment in a dc high voltage photoelectron gun, in Proceedings of the 12th International Workshop on Polarized Ion Sources, Targets and Polarimetry (PSTP 2007), Upton, 2007, *AIP Conf. Proc.* 980, 110 (2008).

[27] M. A. A. Mamun, A. A. Elmustafa, M. L. Stutzman, P. A. Adderley, and M. Poelker, Effect of heat treatments and coatings on the outgassing rate of stainless steel chambers, J. Vac. Sci. Technol. A **32**, 021604 (2014).

[28] M. BastaniNejad, A. Elmustafa, E. Forman, J. Clark, S. Covert, J. Grames, J. Hansknecht, C. Hernandez-Garcia, M. Poelker, and R. Suleiman, Improving the performance of stainless-steel dc high voltage photoelectron gun cathode electrodes via gas conditioning with helium or krypton, Nucl. Instrum. Methods Phys. Res., Sect. A **762**, 135 (2014).

[29] J. Hansknecht, P. Adderley, M. L. Stutzman, and M. Poelker, Sensitive ion pump current monitoring using an inhouse built ion pump power supply, AIP Conf. Proc. **1149**, 1143 (2009).

[30] CST Microwave Studio, http://www.cst.com.

[31] I. Bazarov, L. Cultrera, A. Bartnik, B. Dunham, S. Karkare, Y. Li, X. Liu, J. Maxson, and W. Roussel, Thermal emittance measurements of a cesium potassium antimonide photocathode, Appl. Phys. Lett. **98**, 224101 (2011).

[32] L. Zheng, J. Shao, Y. Du, J. G. Power, E. E. Wisniewski, W. Liu, C. E. Whiteford, M. Conde, S. Doran, C. Jing, C. Tang, and W. Gai, Overestimation of thermal emittance in solenoid scans due to coupled transverse motion, Phys. Rev. Accel. Beams **21**, 122803 (2018).

[33] D. Dowell, I. Bazarov, B. Dunham, K. Harkay, C. Hernandez-Garcia, R. Legg, H. Padmore, T. Rao, J. Smedley, and W. Wan, Cathode R&D for future light sources, Nucl. Instrum. Methods Phys. Res., Sect. A **622**, 685 (2010).

[34] J. Grames, R. Suleiman, P. A. Adderley, J. Clark, J. Hansknecht, D. Machie, M. Poelker, and M. L. Stutzman, Charge and fluence lifetime measurements of a dc high voltage GaAs photogun at high average current, Phys. Rev. ST Accel. Beams **14**, 043501 (2011).

[35] E. Pozdeyev, Ion trapping and cathode bombardment by trapped ions in dc photoguns, Phys. Rev. ST Accel. Beams **10**, 083501 (2007).

[36] S. Full, A. Bartnik, I. V. Bazarov, J. Dobbins, B. Dunham, and G. H. Hoffstaetter, Detection and clearing of trapped ions in the high current Cornell photoinjector, Phys. Rev. Accel. Beams **19**, 034201 (2016).

[37] R. R. Mammei, R. Suleiman, J. Feingold, P. A. Adderley, J. Clark, S. Covert, J. Grames, J. Hansknecht, D. Machie, M. Poelker, T. Rao, J. Smedley, J. Walsh, J. L. McCarter, and M. Ruiz-Osés, Charge lifetime measurements at high average current using a K_2CsSb photocathode inside a dc high voltage photogun, Phys. Rev. ST Accel. Beams **16**, 033401 (2013).

[38] T. Kalvas, O. Tarvainen, T. Ropponen, O. Steczkiewicz, J. Ärje, and H. Clark, IBSIMU: A three-dimensional simulation software for charged particle optics, Rev. Sci. Instrum. **81**, 02B703 (2010).

[39] C. A. Valerio-Lizarraga, I. Leon-Monzon, and R. Scrivens, Negative ion beam space charge compensation by residual gas, Phys. Rev. ST Accel. Beams **18**, 080101 (2015).

[40] C. A. Valerio-Lizarraga, Emittance growth due to space charge compensation and beam intensity instabilities in negative ion beams, Phys. Rev. Accel. Beams **21**, 030101 (2018).

[41] K. Flottmann, ASTRA particle tracking code, https://www.desy.de/~mpyflo/.

[42] K. Halbach and R. Holsinger, SUPERFISH: A computer program for evaluation of rf cavities with cylindrical symmetry, Lawrence Berkley National Laboratory, LBNL Report No. LBL-5040, 1976, https://escholarship.org/uc/item/1d26z7d0#main.

Correction: The names and affiliations of the second and nineteenth through twenty-second authors were missing in the original publication and have been inserted. Missing support information in the Acknowledgments section has been inserted.